

An Improved Quantum Molecular Dynamics Model and its Applications to Fusion Reaction near Barrier *

Ning Wang¹, Zhuxia Li^{1,2,3}, Xizhen Wu^{1,2}

1) *China Institute of Atomic Energy, P. O. Box 275(18), Beijing 102413, P. R. China*

2) *Nuclear Theory Center of National Laboratory of Heavy Ion Accelerator, Lanzhou P. R. China*

3) *Institute of Theoretical Physics, Chinese Academic of Science, Beijing 100080 P. R. China*

Abstract

An improved Quantum Molecular Dynamics model is proposed. By using this model, the properties of ground state of nuclei from ${}^6\text{Li}$ to ${}^{208}\text{Pb}$ can be described very well with one set of parameters. The fusion reactions for ${}^{40}\text{Ca}+{}^{90}\text{Zr}$, ${}^{40}\text{Ca}+{}^{96}\text{Zr}$ and ${}^{48}\text{Ca}+{}^{90}\text{Zr}$ at energy near barrier are studied by this model. The experimental data of the fusion cross sections for ${}^{40}\text{Ca}+{}^{90,96}\text{Zr}$ at the energy near barrier can be reproduced remarkably well without introducing any new parameters. The mechanism for the enhancement of fusion probability for fusion reactions with neutron-rich projectile or target is analyzed.

PACS numbers: 25.70.-z, 24.10.-i

1. INTRODUCTION

*Supported by National Natural Science Foundation of China, No. 19975073, 10175093, 10175089 and Science Foundation of Chinese Nuclear Industry and Major State Basic Research Development Program and Contract, No. G20000774.

E-Mail: wangning@iris.ciae.ac.cn(Ning Wang),lizwux@iris.ciae.ac.cn(Zhuxia Li and Xizhen Wu)

Heavy ion fusion reactions at energies below and near the Coulomb barrier have received considerable attention. The dynamical mechanism of fusion reactions such as the dynamical process of target and projectile deformation before contact and the neck formation and development after contact are of special interest. The Quantum Molecular Dynamics model (QMD) is a microscopic dynamical model and can successfully provide quite a lot of dynamic information about reaction mechanism (for example see [1–3]). However, it is still of difficulties to apply QMD to low energy reactions. The main difficulty for this case is that one has to deal with a problem of time evolution of nuclear many body systems which are of Fermionic nature. On quantum mechanical level, the wave function must be antisymmetrized because of the Fermionic nature of the nuclear constituents, such as did in Antisymmetrized Molecular Dynamics(AMD) [4] and Fermionic Molecular Dynamics (FMD) [5]. AMD and FMD has made a great achievement on describing the nuclear reaction and structure for light nuclei. Nevertheless, for AMD and FMD one has to deal with $N!$ components to the wave function even for a single Slater determinant. Therefore the time evolution by numerically propagating the nuclear wave function would be computationally very demanding and the CPU time necessary to work out calculations for systems with total mass larger than 200 is very large for practical studies [6]. So one is forced to make a compromise between approximating the many body physics and producing a simulation which can execute fast enough to do practical studies. In QMD model, each nucleon is represented by a coherent state of the form ϕ_i and the total N -body wave function is assumed to be the direct product of coherent states, $\Phi = \prod \phi_i$. So QMD calculation is much easier and faster to be carried out. Of course, it is clear that QMD model does not use a Slater determinant and thus antisymmetrization is neglected, although the two-body collisions with Pauli blocking have some effects to maintain a part of Fermionic feature of systems. In fact, two-body collisions are very rare in ground states or in fusion reactions. To compensate this shortcoming, the two-body Pauli potential is introduced by several authors [7–10] to mimic the Pauli principle. Although the Pauli potential can improve the ground states to a certain extent, it is not effective enough to avoid from evolving the initial phase space distribution

obtained from sampling the nuclear ground state density to a classical Boltzmann one after a long time [6].

In addition, the width of Gaussian wave packet in QMD model is taken to be a constant but we find the values adopted are quite different for different calculations. For example, in [3] the Gaussian wave packet width was taken as $L = 4.33 fm^2$ for reaction Ca+Ca and $L = 8.66 fm^2$ for Au+Au. And in ref. [11], the authors took two different values of the width of Gaussian wave packet for multifragmentation and fusion reaction. Therefore it seems to us that it is worthwhile to make further study on the influence of the width of Gaussian wave packet in QMD model calculation.

Aiming at studying the dynamical process of fusion reaction at the energy near barrier one needs quite stable target and projectile nuclei which can bound nucleons for long enough time without spurious particle emission since fusion reaction processes usually last long time. It seems to be difficult for the normal QMD model and an improved QMD model is required for this purpose.

Based on above discussions we develop an improved QMD model in this work. With this model, not only the bulk properties of the ground state of nuclei including density and momentum distribution, binding energy, mean square radius etc. but also their time evolution can be described correctly. And simultaneously we apply it to describing fusion reactions at the energy near barrier and a good agreement with experiment results is achieved.

The structure of the article is as follows: In the section 2, we introduce our improved QMD model. Then we make application of this model to describing the nuclear ground states and the fusion reaction process. The results are presented in section 3. Finally a short summary and conclusion is given in section 4.

2. THE IMPROVED QMD MODEL

In this section we introduce the improved QMD model in more details. First, a brief introduction to QMD model is presented. Then, the main improvements are introduced and their effects are analyzed. Finally, the preparation procedure of initial nuclei is given.

2.1 The Brief Introduction

In QMD, each nucleon is represented by a coherent state of a Gaussian wave packet,

$$\phi_i(\mathbf{r}) = \frac{1}{(2\pi\sigma_r^2)^{3/4}} \exp\left[-\frac{(\mathbf{r} - \mathbf{r}_i)^2}{4\sigma_r^2} + \frac{i}{\hbar}\mathbf{r} \cdot \mathbf{p}_i\right], \quad (1)$$

Where, $\mathbf{r}_i, \mathbf{p}_i$, are the centers of i-th wave packet in the coordinate and momentum space, respectively. σ_r represents the spatial spread of the wave packet. The total N-body wave function is assumed to be the direct product of these coherent states. Through Wigner transformation of the wave function, the N-body phase space distribution function is given by:

$$f_i(\mathbf{r}, \mathbf{p}) = \sum_i \frac{1}{(\pi\hbar)^3} \exp\left[-\frac{(\mathbf{r} - \mathbf{r}_i)^2}{2\sigma_r^2} - \frac{2\sigma_r^2}{\hbar^2}(\mathbf{p} - \mathbf{p}_i)^2\right]. \quad (2)$$

The density and momentum distribution of a system respectively reads as:

$$\rho(\mathbf{r}) = \int f(\mathbf{r}, \mathbf{p}) d^3p = \sum_i \rho_i(\mathbf{r}), \quad (3)$$

$$g(\mathbf{p}) = \int f(\mathbf{r}, \mathbf{p}) d^3r = \sum_i g_i(\mathbf{p}), \quad (4)$$

where the sum runs over all particles in the system, and $\rho_i(\mathbf{r})$ and $g_i(\mathbf{p})$ are the density and momentum distribution of nucleon i:

$$\rho_i(\mathbf{r}) = \frac{1}{(2\pi\sigma_r^2)^{3/2}} \exp\left[-\frac{(\mathbf{r} - \mathbf{r}_i)^2}{2\sigma_r^2}\right], \quad (5)$$

$$g_i(\mathbf{p}) = \frac{1}{(2\pi\sigma_p^2)^{3/2}} \exp\left[-\frac{(\mathbf{p} - \mathbf{p}_i)^2}{2\sigma_p^2}\right], \quad (6)$$

where σ_r and σ_p are the widths of wave packets in coordinate and momentum space, respectively and they satisfy the minimum uncertainty relation:

$$\sigma_r\sigma_p = \frac{\hbar}{2}. \quad (7)$$

In QMD, the nucleons in a system move under the selfconsistently generated mean-field, and the time evolution of $\mathbf{r}_i, \mathbf{p}_i$ is governed by Hamiltonian equation of motion:

$$\dot{\mathbf{p}}_i = -\frac{\partial H}{\partial \mathbf{r}_i}, \dot{\mathbf{r}}_i = \frac{\partial H}{\partial \mathbf{p}_i}. \quad (8)$$

The Hamiltonian H consists of the kinetic energy and effective interaction potential energy,

$$H = T + U, \quad (9)$$

$$T = \sum_i \frac{\mathbf{p}_i^2}{2m}. \quad (10)$$

The effective interaction potential energy includes the nuclear local interaction potential energy and Coulomb interaction potential energy,

$$U = U_{loc} + U_{coul}. \quad (11)$$

And

$$U_{loc} = \int V_{loc} d^3 \mathbf{r}, \quad (12)$$

V_{loc} is the potential energy density and can be derived directly from a zero-range Skyrme interaction [7,12].

$$V_{loc} = \frac{\alpha}{2} \frac{\rho(\mathbf{r})^2}{\rho_0} + \frac{\beta}{3} \frac{\rho(\mathbf{r})^3}{\rho_0^2} + \frac{C_s}{2} \frac{(\rho_p(\mathbf{r}) - \rho_n(\mathbf{r}))^2}{\rho_0} + \frac{g_1}{2} (\nabla \rho(\mathbf{r}))^2. \quad (13)$$

By using

$$\langle Q \rangle_i = \int \rho_i(\mathbf{r}) Q d^3 \mathbf{r}, \quad (14)$$

the nuclear local interaction potential energy can be written as:

$$U_{loc} = \frac{\alpha}{2} \sum_i \langle \frac{\rho}{\rho_0} \rangle_i + \frac{\beta}{3} \sum_i \langle \frac{\rho^2}{\rho_0^2} \rangle_i + \frac{C_s}{2} \int \frac{(\rho_p - \rho_n)^2}{\rho_0} d^3 \mathbf{r} + \int \frac{g_1}{2} (\nabla \rho)^2 d^3 \mathbf{r}. \quad (15)$$

Because of the Gaussian form of density distributions in Eq.(5), all of the integrals in Eq.(12) can be done analytically, furthermore all but one of the sums involves only N^2 terms. The problem in Eq.(15) is that $\sum_i \langle \frac{\rho^2}{\rho_0^2} \rangle_i$ is of order of N^3 and for a system of hundreds of

particles, evaluation of N^3 elements is very time-consuming and computationally prohibitive, so it is approximated by [7]

$$\sum_i \langle \frac{\rho^2}{\rho_0^2} \rangle_i \approx \sum_i \langle \frac{\rho}{\rho_0} \rangle_i^2 + \int \frac{g_2}{2} (\nabla \rho)^2 d^3 \mathbf{r}, \quad (16)$$

which is a N^2 operation. Since the second term in Eq.(16) has the same functional form as the surface energy term in Eq.(15), we combine them into one term and call it the surface energy term with parameter $g_0 = g_1 + g_2$. The Coulomb potential energy is obtained from:

$$U_{coul} = \frac{1}{2} \sum_{i \neq j} \int \rho_i(\mathbf{r}) \frac{e^2}{|\mathbf{r} - \mathbf{r}'|} \rho_j(\mathbf{r}') d^3 \mathbf{r} d^3 \mathbf{r}'. \quad (17)$$

The parameters in this work are listed in Table.1.

Table. 1

2.2 The Effect of Surface Energy Term and Phase Space Constraint

It is obvious that the surface effects are important for a finite system. Let us first study the effects of the term $U_{surface} = \frac{g_0}{2} \int (\nabla \rho)^2 d^3 r$. In Fig.1, we show a schematic figure of the effect of the surface energy term. As mentioned in the introduction, the initial density distribution of a system will evolve to a classical one according to classical equations of motion after long enough time. Suppose we have a Gaussian form of density distribution as shown in Fig.1(a). With this density distribution, the surface energy term $U_{surface}$ is obtained by definition, and its shape is shown in Fig.1(b). From the figure we can see that the particles in the central region will experience a repulsion and are forced to move toward outside. Consequently, the density at central region is suppressed and avoids going up unreasonable high. While the particles at surface feel an attraction and move toward inside so that the density distribution at the surface will not extend too far. Fig.1(c) shows the influence of the surface energy term on the density distribution of the system. The solid curve and dashed curve are the density distribution calculated with and without the surface term taken into account, respectively. It is clear that the density distribution calculated with the surface term is more reasonable than that without the surface term.

Fig. 1

As is well known, the Gaussian wave packet itself has a long tail which makes the surface of the system more disperse. Therefore, in QMD model it is more important to introduce the surface energy term. Here we pay great attention to the surface energy term, and make further study about the effect of the surface term for realistic cases. In Fig.2 and Fig.3 we show the time evolution of the density distribution of ^{90}Zr calculated without and with surface term taken into account. The initial density distribution is obtained by relativistic mean field theory (RMF) calculation [13]. When the surface term is not included, as Fig.2 shows, the density distribution keep stable and the central density of nuclei maintains lower than 0.2fm^{-3} only at the early stage(for example, see $t = 5\text{fm}/c$)for all runs. With further time evolution, the density distribution changes and deviates from the initial one. After about $t = 200\text{fm}/c$, the central density begins to go up, and at about $t = 400\text{fm}/c$ the central density even reaches 0.3fm^{-3} . And after $t = 400\text{fm}/c$ there is spurious emission of nucleons while the central density is still too high. When the surface term is included, as Fig.3 shows, with time evolution the shape of density distribution can keep remarkably stable as the same as the initial one, and the central density always keeps at $\rho = 0.165\text{fm}^{-3}$. Even at $t = 800\text{fm}/c$, the central density still remains the same value of $\rho = 0.165\text{fm}^{-3}$. From the comparison of these two figures, one can clearly see that the surface term is effective to maintain a reasonable density distribution for a ground state of nucleus during time evolution.

Fig. 2

Fig. 3

Similarly, the momentum distribution will evolve to a classical distribution from initial momentum distribution after long time. To avoid it, a phase space density constraint was introduced by Papa et. al. in ref. [6]. Because Fermionic nature requires one-body phase space density of a system $\bar{f}_i \leq 1$, in this work we perform many body elastic scattering to

reduce the phase space occupation if the phase space occupation \bar{f}_i is greater than 1, as did in ref. [6]. At the same time the Pauli blocking probability is checked like the usual treatment in two-body collision process. This kind of constraint affects the low momentum part of the momentum distribution strongly and can effectively avoid the number of particles with low momentum becoming too large. Fig.4 shows the comparison of the time evolution of the average momentum distributions calculated without taking constraint (dashed curves) and with taking constraint (solid curves) for 200 ^{208}Pb nuclei. Here the momentum distribution means the distribution of the centroid momentums of wave packets of nucleons in a system. From the figure one can see that at the initial time, the momentum distribution (dash dotted curves) is reasonable. With time evolution, the difference in the momentum distributions for two cases becomes obvious. When the phase space density constraint is not taken into account, the number of particles with low momentum increases greatly and the momentum distribution deviates from the initial one clearly, as shown in dashed curves. This problem is usually ignored in the QMD calculation when it is applied to medium or high energy reactions. However for describing ground state or fusion reactions near barrier, this problem should be considered seriously. From solid curves one can find the behavior of time evolution of momentum distribution, especially the low momentum part is improved a lot after taking the phase space density constraint into account. However we notice that the high momentum part of the distribution is still too disperse comparing with the initial one. This means that phase space constraint is still not enough to control the momentum distribution as good as request. But even so we find that it improves the fusion reaction near barrier a lot. It may be because the high momentum part is not so important for this case. The investigating on further improvement of the behavior of the time evolution of momentum distribution is in progress.

Fig. 4

2.3 The Width of Wave Packet

In QMD, the width of wave packet can be regarded as a quantity having relations with the interaction range of a particle. Its influence disappears for infinite nuclear matter whereas for finite systems it may play a un-negligible role [3]. In the normal QMD model, the width of wave packet is taken as a constant. For example, in ref. [14], the width of wave packet is taken as $\sigma_r = 1.04fm$ for Ca+Ca, and $\sigma_r = 1.47fm$ (i.e. $L = 8.66fm^2$ in notation of [14]) for Au+Au. Here let us study the influence of the width of wave packet on the stability of a nuclear system. As an example, for the ground state of ^{208}Pb , if we choose $\sigma_r = 1.04fm$, there are about 30 spurious particles emitted until $800fm/c$ while if $\sigma_r = 1.44fm$, there are no particles emitted until $800fm/c$ generally and simultaneously both the density and momentum distribution are reasonable. In heavy ion reactions, if spurious emission becomes serious, the result will be affected obviously. Therefore in the study of reaction of Au+Au in ref. [14], a larger width of wave packet was taken, i.e. $\sigma_r = 1.47fm$, and we find it is reasonable and necessary. In fusion reaction at energy near barrier, the reaction process lasts a long time, therefore in QMD calculations, to make nuclei stable enough is vital to the result for fusion reactions. On the other hand, for Ca or lighter nuclei, if a large width of wave packet is adopted, the fluctuation of mean square root of radius of the system becomes too large during time evolution, which is obviously not suitable. Therefore for Ca+Ca system, for example in ref. [14] a small wave packet width such as $\sigma_r = 1.04fm$ was adopted. In addition, we also find that it is very important to take a reasonable value of wave packet width in order to describe the Coulomb barrier correctly. We will show it in section 3. Based on above discussion we propose a system size dependent wave packet width. In our present work, we take the dependence of the wave packet width on system size as:

$$\sigma_r = 0.16N_A^{1/3} + 0.49, \quad (18)$$

where N_A is the number of nucleons binding in a system A which can be a individual nucleus, or clusters or a compound nucleus produced in heavy ion reactions according to the specific problem studied. After introducing the system size dependent wave packet width, our model is expected be able to well describe the bulk properties of nuclei in a wide mass region from

${}^6\text{Li}$ to ${}^{208}\text{Pb}$ as well as the behavior of fusion process.

2.4 Preparation of Initial Nuclei

As is well known, the initial condition is very important in QMD calculations. In the present work, the preparation of initial nuclei is as follow:

Firstly, the neutron and proton density distributions of nuclei are obtained by means of RMF calculations. Then the position of each nucleon in nuclei is sampled according to the density distribution obtained.

Secondly, based on the density distribution obtained above, the Fermi momentum P_F is calculated by the local density approximation. Considering the momentum of each nucleon being also represented by a wave packet with a width of σ_p which satisfies the minimum uncertainty relation $\sigma_r\sigma_p = \frac{\hbar}{2}$, the Fermi momentum P'_F adopted in the sampling of the momentums of nucleons should be smaller than P_F . Here we take the difference $\Delta P_F = P_F - P'_F$ to be about the width of half height of Guassian wave packet in momentum space (see expression(6)). For some light nuclei (mass is less than 16) we make a slight adjustment of the difference ΔP_F which is less than tenth of ΔP_F . Thus we can prepare the initial nuclei from ${}^6\text{Li}$ to ${}^{208}\text{Pb}$ of which the binding energies and mean square radius are in good agreement with experimental data.

It is important to have stable initial nuclei with no spurious particle emission. To check the stability of the pre-prepared initial nuclei, we let the pre-prepared nuclear systems evolve for at least 600fm/c, then the ground state properties including mean square radius, binding energy, density distribution, momentum distribution, phase space distribution, etc. are checked elaborately. Only those pre-prepared nuclei for which the bulk properties are good enough, the behavior of the time evolution of all these properties maintain stable and there is no spurious particle emission are selected as 'good initial nuclei' and are stored for usage in simulating reactions.

3. RESULTS

3.1 Properties of Ground State

In Table.2 we give the calculated results of binding energy and mean square root of radii for ${}^6\text{Li}$, ${}^{16}\text{O}$, ${}^{30}\text{P}$, ${}^{40}\text{Ca}$, ${}^{90}\text{Zr}$, ${}^{108}\text{Ag}$, ${}^{144}\text{Nd}$, ${}^{197}\text{Au}$ and ${}^{208}\text{Pb}$. The binding energies are compared with experimental data and the mean square roots of radii are compared with the empirical formula [15]

$$\langle r^2 \rangle^{1/2} = 0.82A^{1/3} + 0.58. \quad (19)$$

Table. 2

One can see that the calculated binding energies are in good agreement with experimental data and the mean square roots of radii are also in good agreement with empirical values obtained from the empirical formula(19) except for small nuclei. For small nuclei, our results are a little bit better than the empirical formula when we compare them with experimental data(see ref.12). Considering how few parameters we use in this model, the obtained results in describing the ground state properties of nucleus are quite satisfied. In addition to fulfilling the static properties of ground state of nuclei, such as the binding energies, the mean square roots of radii, the behavior of the time evolution of those quantities are also very concerned. In Fig.5 we show the time evolution of the binding energies and mean square roots of radii of ${}^{16}\text{O}$, ${}^{40}\text{Ca}$, ${}^{90}\text{Zr}$ and ${}^{208}\text{Pb}$. One can see that for these nuclei the binding energy and mean square roots of radii can maintain stable for at least $600\text{fm}/c$. One can also find that the larger the size of nucleus is, the smaller the fluctuation of binding energy and mean square root of radius with time evolution is, which is because the mean field effect becomes stronger as system size increases.

Fig. 5

3.2 Coulomb Barrier

Coulomb barrier is a very important quantity in describing fusion reactions. It's height and width are two sensitive parameters in WKB calculations of fusion cross sections. The Coulomb barrier can be calculated microscopically using the following expression in QMD,

$$V_b(r) = \int d^3r_1 \int d^3r_2 \rho_1(\mathbf{r}_1 - \mathbf{r}_{1c}) V(\mathbf{r}_1 - \mathbf{r}_2) \rho_2(\mathbf{r}_2 - \mathbf{r}_{2c}), \quad (20)$$

where ρ_1 , ρ_2 are the density distribution of projectile and target nuclei, respectively, \mathbf{r}_{1c} , \mathbf{r}_{2c} are their centers of mass, respectively. $r = |\mathbf{r}_{1c} - \mathbf{r}_{2c}|$ is the distance of projectile and target nuclei. In QMD both static and dynamic Coulomb barrier can be calculated. For calculating the static Coulomb barrier of fusion reaction, the static density distributions of both projectile and target are taken. In the present work, we first let the initial projectile and target nuclei evolve individually under their self-consistent mean field for about 300fm/c. Then, we take the density distribution at this time as the static density distribution to calculate static Coulomb barrier. The dynamical Coulomb barrier is the barrier experienced during the fusion process and is calculated based on the instantaneous density distribution of the system in the real reaction process.

Fig.6 shows the average static Coulomb barrier of $^{40}\text{Ca}+^{90}\text{Zr}$ fusion reactions. The solid curve denotes the result of our improved QMD model, the crossed curve denotes the result of proximity potential [16]. One can see that two results by using two quite different models agree with each other remarkably well except for the case when two nuclei overlapping happens. The reason for this deviation is that the proximity potential is only applicable to the case when two nuclei do not overlap and so as soon as the projectile and target overlap it may not be able to give accurate result any more. While QMD model is a microscopic model and can be applicable to both cases without and with overlapping of two nuclei.

Fig. 6

In order to study the effect of the system size dependence of wave packet width on Coulomb barrier, in Fig.7 we show the static Coulomb barrier for $^{40}\text{Ca}+^{90}\text{Zr}$ system calculated by fixed wave packet widths and the system size dependent wave packet width. The

dashed curve denotes the calculated results with fixed wave packet width $\sigma_r = 1.3fm$ [6] and the solid curve denotes the results with system size dependent wave packet width given by expression(18). For $\sigma_r = 1.3fm$ case, the Coulomb barrier calculated by QMD is lower than that of the case with size dependent wave packet width. In this figure, we find that the wave packet width of nucleon affects the density distribution of the system and thus affects the Coulomb barrier considerably. Fig.6 and Fig.7 show us that it is important to introduce the system size dependent wave packet width for describing Coulomb barrier correctly.

Fig. 7

3.3 Fusion Reaction

After performing the procedure of preparation of initial nuclei as mentioned in the previous section, from thousands of pre-prepared systems, we elaborately select 10 projectile nuclei and 10 target nuclei. By rotating these prepared projectile and target nuclei around their centers of mass by an Euler angle chosen randomly, we create 100 bombarding events for each reaction energy E and impact parameter b . Through counting the number of fusion events, we obtain the probability of fusion reaction $g_{fus}(E, b)$, then the cross section is calculated by using the expression:

$$\sigma_{fus} = 2\pi \int_0^{b_{max}} bg_{fus}(E, b)db = 2\pi \sum bg_{fus}(E, b)\Delta b. \quad (21)$$

The distance from projectile to target at initial time is taken to be $l = 20fm$.

The definition of fusion in QMD model is still a difficult problem which needs to consider carefully. In TDHF calculations, the fusion event is defined rather operationally as the event in which the coalesced one-body density survives through one or more rotations of composite system or through several oscillations of its radius. In this work we also use the same definition of fusion event with that in TDHF calculations. In addition, considering the specific feature of QMD calculations, if the event in which one or several nucleons escape prior to the formation of compound nucleus is still belong to fusion event [10]. Here, for an

event if the number of nucleons escaped during the process of forming compound nuclei is equal or less than 6, we consider the event as fusion event.

Fig.8 shows the fusion cross sections for (a) $^{40}\text{Ca}+^{90}\text{Zr}$ and (b) $^{40}\text{Ca}+^{96}\text{Zr}$, respectively. Experimental data are taken from ref. [17]. One can see that the calculation results with our improved QMD model agree with the experimental data remarkably well for both $^{40}\text{Ca}+^{90}\text{Zr}$ and $^{40}\text{Ca}+^{96}\text{Zr}$. Neither adjusting parameters nor adding some special reaction channels for neutron-rich nuclei(see ref. [18]) are needed in our calculations. It implies that our improved QMD model is quite successful in describing the fusion reaction near barrier for both nuclei at β stable line and neutron-rich nuclei. In order to investigate the effect of neutron-rich projectile on fusion probability in Fig.9 we show the fusion cross sections of $^{48}\text{Ca}+^{90}\text{Zr}$. One can see a even stronger enhancement of fusion cross sections in this case.

Fig. 8

Fig. 9

From the comparison of the fusion cross sections for $^{40}\text{Ca}+^{90}\text{Zr}$, $^{40}\text{Ca}+^{96}\text{Zr}$ and $^{48}\text{Ca}+^{90}\text{Zr}$, one can easily find that there is a strong enhancement of fusion cross section for neutron-rich nuclear reactions. In order to study the mechanism of the enhancement of fusion cross sections for neutron-rich nuclear reactions, we study the height of dynamic Coulomb barrier V_b , the potential well of compound nuclei $V_{com.}$ and as well as the neutron and proton density distribution of the compound nuclei. Here the height of dynamic Coulomb barrier means the height of the highest Coulomb barrier experienced during the path of fusion. The method of calculating dynamic Coulomb barrier is given in section 3.2. The potential well of compound nuclei can be calculated by the following expression:

$$V_{com.}(\mathbf{r}') = \int \rho_{com.}(\mathbf{r})V(\mathbf{r} - \mathbf{r}')d^3\mathbf{r}, \quad (22)$$

where $\rho_{com.}(\mathbf{r})$ is the density distribution of the compound nuclei formed in the fusion reaction, and $V(\mathbf{r} - \mathbf{r}')$ is effective nucleon-nucleon interaction. The calculation results for $^{40}\text{Ca}+^{90}\text{Zr}$, $^{40}\text{Ca}+^{96}\text{Zr}$ and $^{48}\text{Ca}+^{90}\text{Zr}$ at $E_{c.m.} = 95.0\text{MeV}, 107.6\text{MeV}$ are listed in Table.3.

Now, let us first discuss the effect of neutron-rich target by comparing reactions $^{40}\text{Ca}+^{90}\text{Zr}$ and $^{40}\text{Ca}+^{96}\text{Zr}$ at energy near barrier. At $E_{c.m.} = 107.6\text{MeV}$, the average height of dynamic Coulomb barrier is about 88.2MeV which is lower than that of static Coulomb barrier of about 98.0MeV , and the average of depth of mean potential well of compound nuclei $V_{com.}$ is about 45.38MeV . Comparing with $^{40}\text{Ca}+^{90}\text{Zr}$ case, one can see that at this energy the height of dynamic Coulomb barrier is almost equal, and the depth of mean potential well of compound nuclei formed in $^{40}\text{Ca}+^{96}\text{Zr}$ is only about 0.3MeV deeper than that in $^{40}\text{Ca}+^{90}\text{Zr}$ which is about 44.92MeV . But as energy decreases, for example, $E_{c.m.} = 95.0\text{MeV}$, the height of dynamic Coulomb barrier for $^{40}\text{Ca}+^{96}\text{Zr}$ is about 80.6MeV and is more than 5MeV lower than that of 85.2MeV for $^{40}\text{Ca}+^{90}\text{Zr}$. While the depth of mean potential well of compound nuclei formed in the fusion process at this energy increases a little comparing with that at $E_{c.m.} = 107.6\text{MeV}$ for both $^{40}\text{Ca}+^{90}\text{Zr}$ and $^{40}\text{Ca}+^{96}\text{Zr}$. From this result, we find that the dynamic Coulomb barrier for reactions with neutron-rich target such as $^{40}\text{Ca}+^{96}\text{Zr}$ decreases more strongly than that for $^{40}\text{Ca}+^{90}\text{Zr}$ as energy decreases from 107.6MeV to 95.0MeV and consequently, it leads to a stronger enhancement of the fusion cross sections for $^{40}\text{Ca}+^{96}\text{Zr}$ at lower energy.

Fig. 10

Now, let us turn to the fusion reaction with neutron-rich projectile, $^{48}\text{Ca}+^{90}\text{Zr}$. Fig.10 shows the comparison between the static and dynamic Coulomb barrier of $^{48}\text{Ca}+^{90}\text{Zr}$ at energy $E_{c.m.} = 95.0\text{MeV}$. The solid curve denotes the static Coulomb barrier, and the dotted curve denotes the dynamic Coulomb barrier. From Fig.10, one can see that in the fusion reaction at near barrier, the dynamic Coulomb barrier is lower than the static Coulomb barrier and the thickness of the barrier decreases largely. Concerning the height of dynamic Coulomb barrier, from Table 3 one can see at energy $E_{c.m.} = 107.6\text{MeV}$, the height of its dynamic Coulomb barrier is about 85.4MeV which is about 3MeV lower than that for both $^{40}\text{Ca}+^{90}\text{Zr}$ and $^{40}\text{Ca}+^{96}\text{Zr}$ cases. And at $E_{c.m.} = 95.0\text{MeV}$, the height of barrier falls about one MeV and is lower than that of $^{40}\text{Ca}+^{90}\text{Zr}$ but higher than that of $^{40}\text{Ca}+^{96}\text{Zr}$.

The depth of mean potential well of the compound nuclei formed in $^{48}\text{Ca}+^{90}\text{Zr}$ is a little deeper than that formed in $^{40}\text{Ca}+^{90}\text{Zr}$. On the other hand, the shape of the mean potential well formed in fusion process may also play an important role for fusion probability. In Fig.11 we show the mean potential wells of compound nuclei formed in $^{40}\text{Ca}+^{90}\text{Zr}$ (the dotted curve), $^{40}\text{Ca}+^{96}\text{Zr}$ (the dashed curve) and $^{48}\text{Ca}+^{90}\text{Zr}$ (the solid curve). From the comparison, one can see that the mean potential well of compound system in $^{48}\text{Ca}+^{90}\text{Zr}$ is obviously wider than the other two cases. And when energy decreases from $E_{c.m.} = 107.6\text{MeV}$ to $E_{c.m.} = 95.0\text{MeV}$, the depth of mean potential well of compound nuclei in $^{48}\text{Ca}+^{90}\text{Zr}$ increases more than the other two cases(see Table.3). In order to understand the reason of forming the different mean potential well for these three different reactions. We show the neutron and proton density distributions of compound nuclei for three cases in Fig.12 in which the dashed curves denote the density distribution of neutrons and the solid curves denote that of protons. From Fig.12 one can see that the proton distribution for reaction $^{48}\text{Ca}+^{90}\text{Zr}$ is different from the other two cases and also there are relatively more neutrons distributed on the surface of compound nuclei. This kind of density distribution seem to have advantage of forming a favorable potential well and leads to a strong enhancement of fusion probability for $^{48}\text{Ca}+^{90}\text{Zr}$.

Table. 3

Fig. 11

Fig. 12

From above comparison of the fusion cross sections for reactions $^{40}\text{Ca}+^{90}\text{Zr}$, $^{40}\text{Ca}+^{96}\text{Zr}$ and $^{48}\text{Ca}+^{90}\text{Zr}$. We find that there is an enhancement of fusion cross sections for reactions with neutron-rich target or projectile resulting from the lowering of dynamic Coulomb barrier or forming a favorable potential well of compound system in fusion process or both. However,

as soon as two nuclei approach with each other their shape could be deformed and after contact a neck will be developed. The fusion cross section can be affected largely by this dynamical process. What is the role played by excess neutrons in neutron-rich projectile and target on this dynamical process? How do protons and neutrons transfer during fusion process? All these problems are very important for understanding the mechanism of fusion reactions. They will be studied in our future work.

CONCLUSION

In this work, we have proposed an improved QMD model. Our improvements mainly include: taking into account the effects of surface term; introducing system size dependent wave packet width; and adopting phase space constraint of $\bar{f}_i \leq 1$. By using this model, the ground state properties including binding energy, mean square root of radius, density distribution, momentum distribution and phase space distribution and so on from ${}^6\text{Li}$ to ${}^{208}\text{Pb}$ can be described very well with one set of parameters. Simultaneously the Coulomb barrier can be described well. By applying our improved QMD model, the experimental data of the fusion cross sections for ${}^{40}\text{Ca}+{}^{90,96}\text{Zr}$ can be reproduced remarkably well without introducing any new parameters. In addition, the fusion reaction at energy near barrier for ${}^{48}\text{Ca}+{}^{90}\text{Zr}$ is studied. We find that there is an enhancement of fusion cross sections for reactions with neutron-rich target or projectile. The mechanism for the enhancement of fusion cross sections in these reactions is the lowering of the dynamic Coulomb barrier or forming the favorable potential well of compound system in fusion process or both. Nevertheless, the problems concerning the neck dynamics and the mass transformation are not the task of this paper. The work about these aspects is on progress.

REFERENCES

- [1] C Hartnack et. al. Nucl.Phys. **A495** (1989) 303.
- [2] J.Aichelin Phys.Rep. **202** (1991), and references therein.
- [3] C Hartnack et. al. Eur.Phys. J. **A 1** (1998) 151.
- [4] A. Ono, H. Horiuchi, Toshiki Maruyama, and A. Ohnishi, Phys. Rev. Letters **68**, (1992)2898; Y. Kanada-En'yo and H. Horiuchi, Phys. Rev. **C52** (1995) 647; and Y. Kanada-En'yo, H. Horiuchi, and A. Doté, Phys. Rev. **C60**(1999) 064304.
- [5] H.Feldmeier, J.Schneck,Prog.Part.Nucl.Phys. **39** (1997)392, and references therein.
- [6] Massimo Papa, Toshiki Maruyama, et al. arXiv:Nucl-th 0012083.
- [7] David H.Boal, James N.Glosi Phys.Rev. **C37** (1988)91, and Phys.Rev.**C38** (1988) 2621.
- [8] L. Wilets, E.M.Henley,et al. Nucl.Phys. **A282** (1977) 341.
- [9] C.O.Dorso, S.Duarte et al. Phys.Lett. **B188** (1987) 287.
- [10] T.Maruyama, K.Niita, et al. Phys.Rev, **C57** (1998) 655.
- [11] Toshiki Maruyama, Aldo Bonasera, Massimo Papa, et al. arXiv:Nucl-th 0107021.
- [12] D.Vautherin, D.M.Brink, Phys.Rev.**C5** (1972) 626.
- [13] P.G.Reinhard, M.Rufa, J.Maruhu, W.Greiner, J.Fridrich Z.Phys. **A323** (1986) 13.
- [14] Ch.Hartnack, et al. arXiv:Nucl-th 9811015.
- [15] M.A.Preston and R.K.Bhaduri, Structure of the Nucleus, Addison-Wesley Publishing Co., Inc., Reading, Mass. (1975) P.10-14.
- [16] W.D.Myers, W.J.Swiatecki, Phys.Rev. **C62** (2000) 044610.
- [17] H.Timmers, et al. Nucl.Phys.**A633** (1998) 421.
- [18] V.Yu.Denisov arXiv:Nucl-th 9809083.

CAPTIONS

Fig.1 The schematic figure of the effect of surface term of interaction potential energy. (a) the density distribution of Boltzmann form. (b) the shape of interaction of surface term, the arrows denote the direction of corresponding force. (c) the comparison between the density distribution calculated with and without surface term taken into account. The solid curve denotes the density distribution with surface term, and the dashed curve denotes that of without surface term.

Fig.2 The time evolution of density distribution of ^{90}Zr without surface term.

Fig.3 The time evolution of density distribution of ^{90}Zr with surface term taken into account.

Fig.4 The time evolution of momentum distribution of ^{208}Pb . The dash-dotted curve denotes the initial momentum distribution which is obtained from the Relativistic Mean Field calculations. The dashed curve denotes the momentum distribution without phase space density constraint taken into account. The solid curve denotes the momentum distribution with constraint.

Fig.5 The time evolution of binding energies and mean square roots of radii of ^{16}O , ^{40}Ca , ^{90}Zr and ^{208}Pb .

Fig.6 The static Coulomb barrier of $^{40}\text{Ca}+^{90}\text{Zr}$ calculated by QMD model and proximity potential. The solid curve denotes the results of QMD model calculation and the crossed curve denotes that of proximity potential, respectively.

Fig.7 The comparison between the static Coulomb barrier of $^{40}\text{Ca}+^{90}\text{Zr}$ calculated with fixed wave packet width (the dashed curve) and the system size dependent wave packet width(the solid curve).

Fig.8 The fusion cross sections for $^{40}\text{Ca}+^{90,96}\text{Zr}$. The experimental data are taken from

[17]. The solid curves denote the results of QMD model and the crossed curves denote the experimental data.

Fig.9 The fusion cross section for $^{48}\text{Ca}+^{90}\text{Zr}$.

Fig.10 The Coulomb barrier for fusion reaction $^{48}\text{Ca}+^{90}\text{Zr}$. The solid curve denotes the static Coulomb barrier and the solid curve with dots denotes the dynamic Coulomb barrier at energy $E_{c.m.} = 95.0\text{MeV}$.

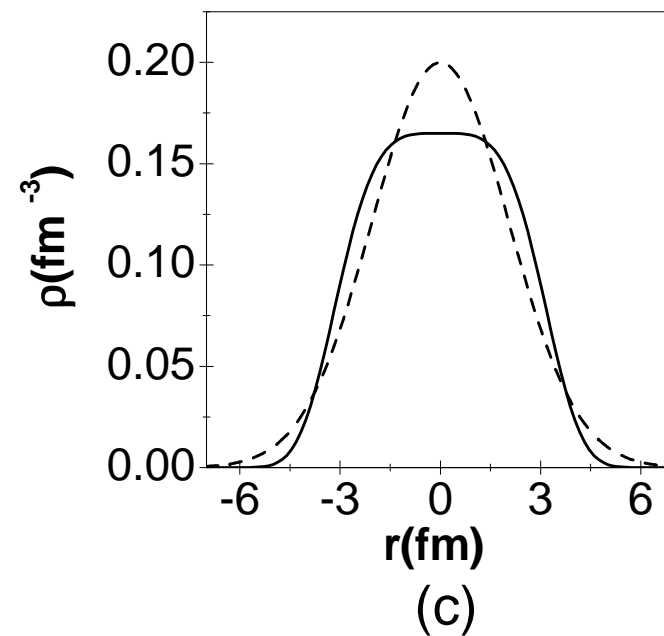
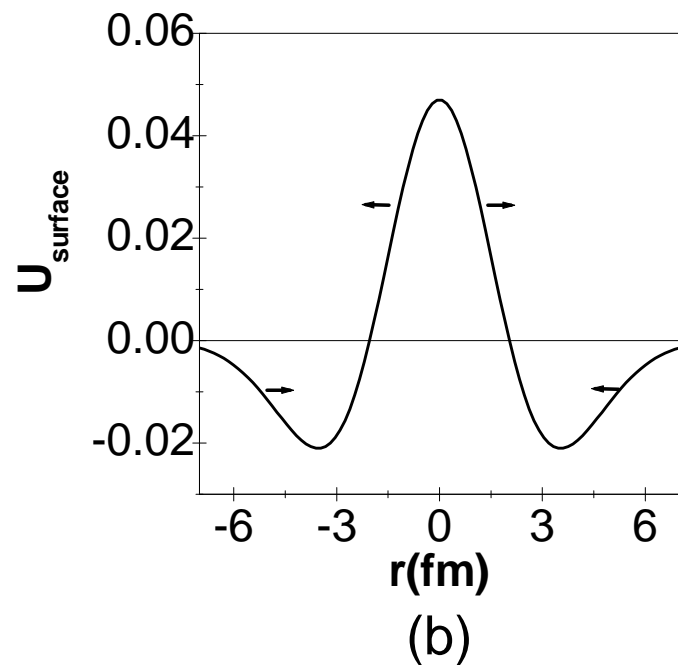
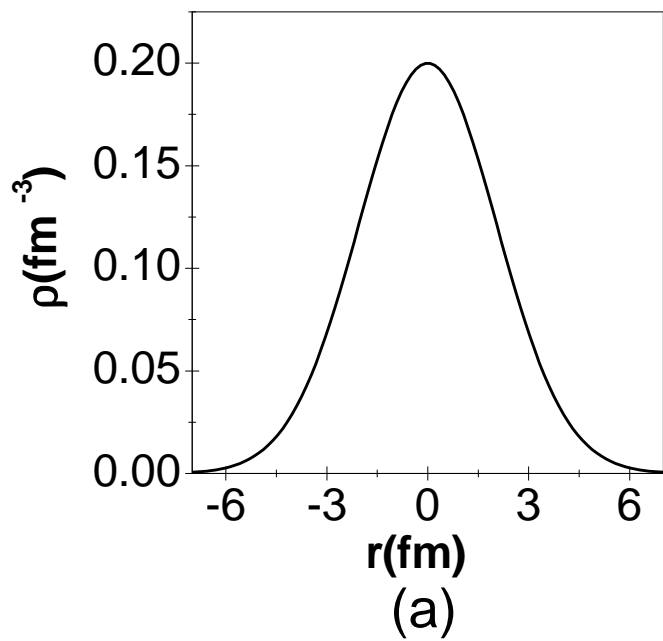
Fig.11 The comparison of mean potential wells of compound nuclei formed in $^{40}\text{Ca}+^{90}\text{Zr}$, $^{40}\text{Ca}+^{96}\text{Zr}$ and in $^{48}\text{Ca}+^{90}\text{Zr}$. The dotted curve denotes the mean potential well of compound nuclei in fusion reaction $^{40}\text{Ca}+^{90}\text{Zr}$, the dashed curve denotes that in reaction $^{40}\text{Ca}+^{96}\text{Zr}$ and the solid curve denotes that in reaction $^{48}\text{Ca}+^{90}\text{Zr}$.

Fig.12 The density distributions of compound nuclei formed in $^{40}\text{Ca}+^{90}\text{Zr}$, $^{40}\text{Ca}+^{96}\text{Zr}$ and $^{48}\text{Ca}+^{90}\text{Zr}$. The dashed curves denote the neutron density distribution and the solid curves denote proton density distribution.

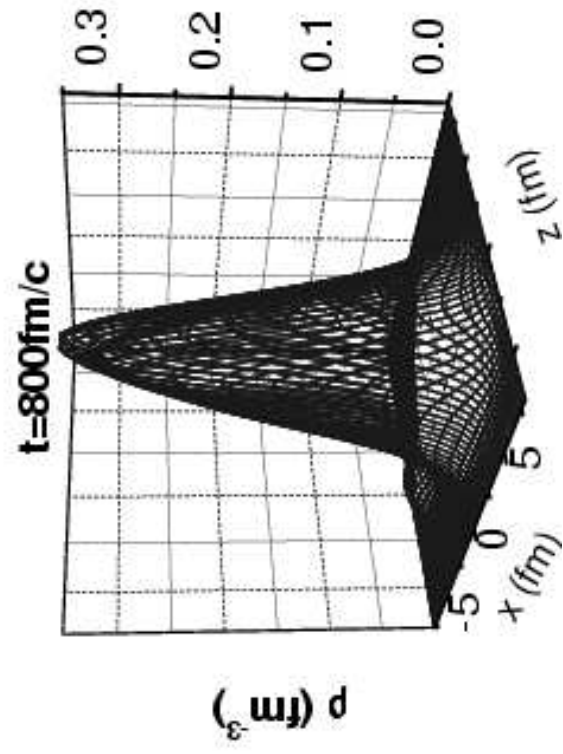
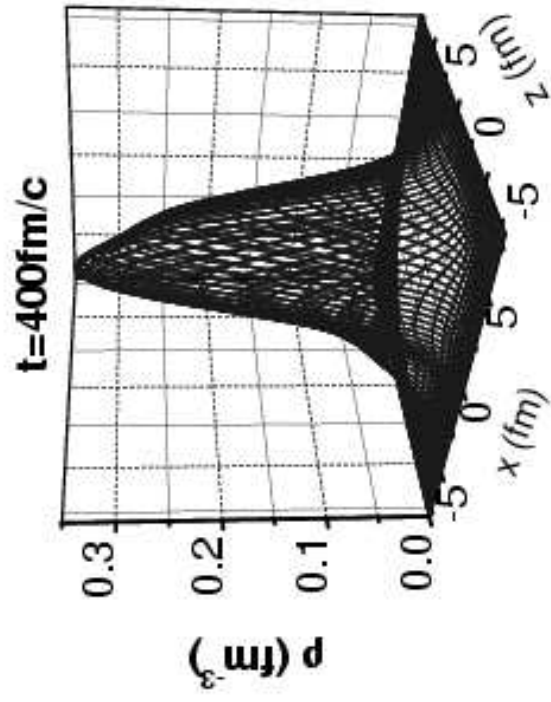
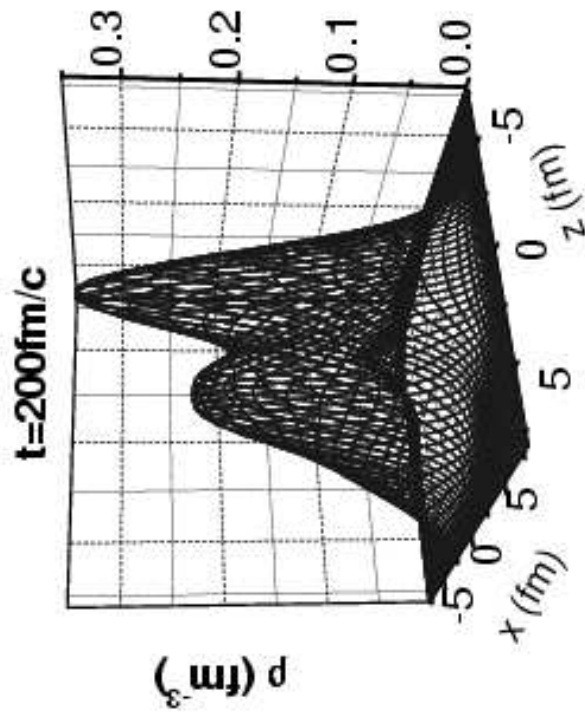
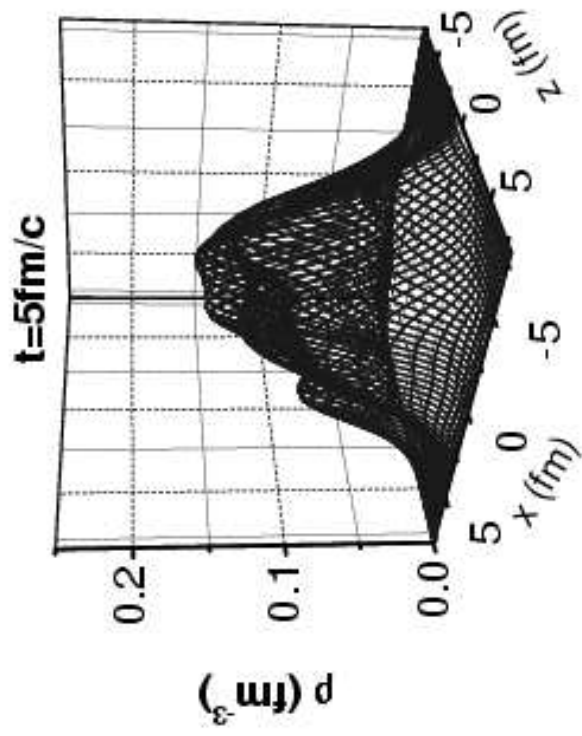
Table.1 The parameters adopted in the present work.

Table.2 The calculating results of binding energies per nucleon and mean square roots of radii for nuclei from ^6Li to ^{208}Pb . The binding energies are compared with the experimental data. The mean square roots of radii are compared with empirical formula [15].

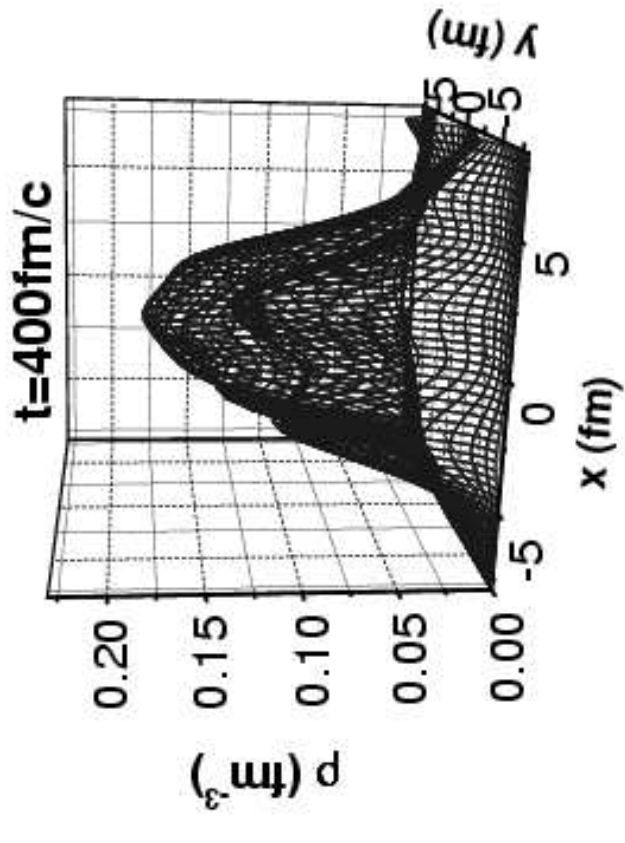
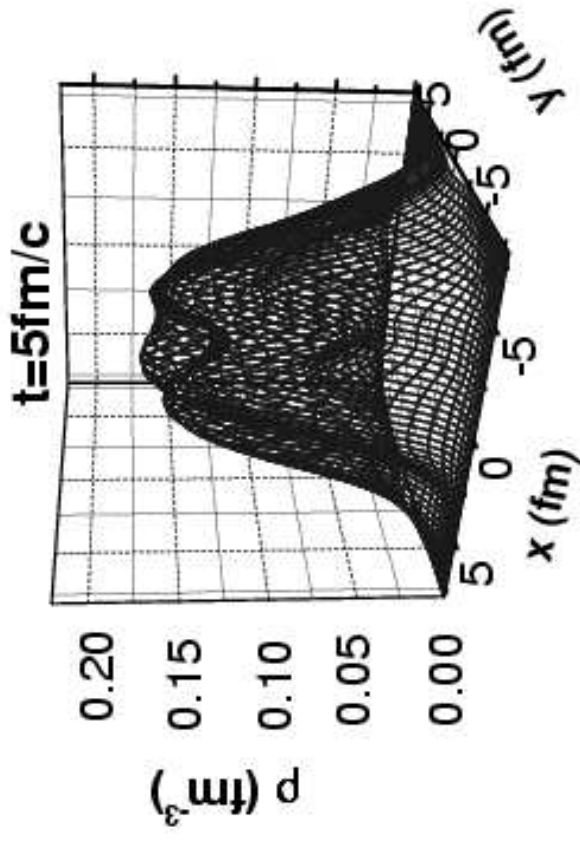
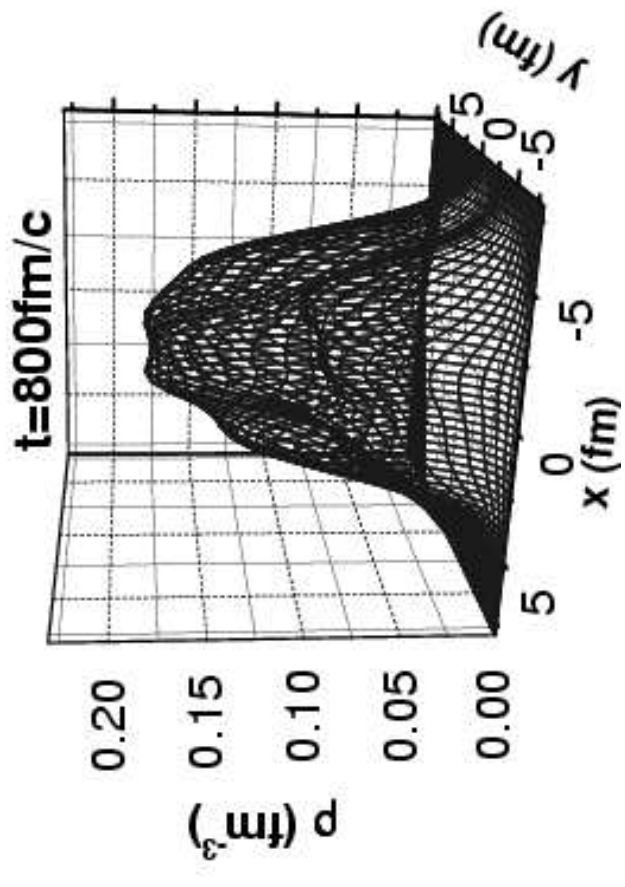
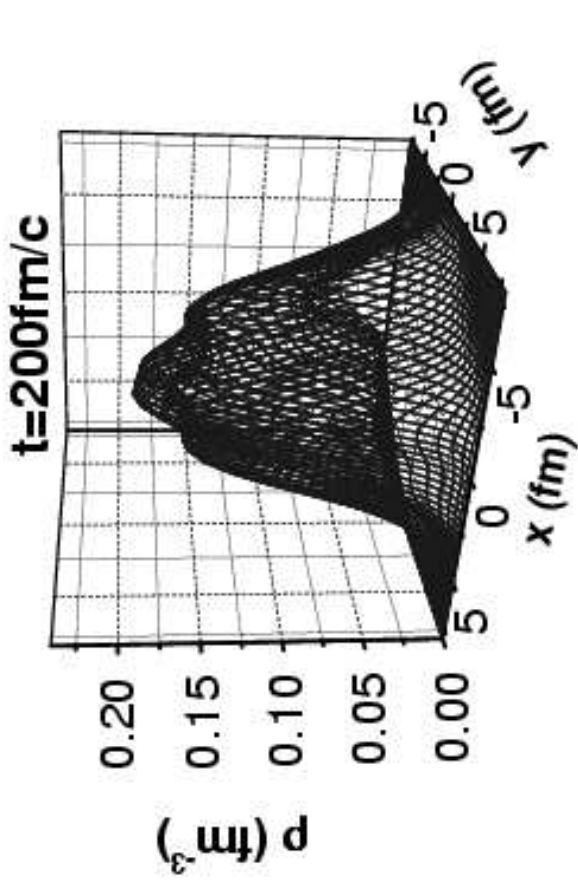
Table.3 The height of dynamic Coulomb barrier and the depth of mean potential wells of compound nuclei in fusion reactions $^{40}\text{Ca}+^{90}\text{Zr}$, $^{40}\text{Ca}+^{96}\text{Zr}$ and $^{48}\text{Ca}+^{90}\text{Zr}$ at $E_{c.m.} = 95.0\text{MeV}$ and $E_{c.m.} = 107.6\text{MeV}$.



$\alpha(\text{GeV})$	$\beta(\text{GeV})$	$\rho_0(\text{fm}^{-3})$	$g_0(\text{GeV fm}^{-5})$	$C_s(\text{GeV})$
-0.124	0.071	0.165	0.96	0.032



Nuclear Name	Binding Energy		Mean Square Radius	
	QMD	Exp.	QMD	Data
⁶ Li	5.78	5.33	2.13	2.07
¹⁶ O	8.01	7.97	2.85	2.64
³⁰ P	8.32	8.35	3.35	3.12
⁴⁰ Ca	8.55	8.55	3.54	3.38
⁹⁰ Zr	8.57	8.71	4.25	4.25
¹⁰⁸ Ag	8.41	8.50	4.47	4.48
¹⁴⁴ Nd	8.25	8.27	4.84	4.87
¹⁹⁷ Au	8.01	7.92	5.30	5.35
²⁰⁸ Pb	7.87	7.87	5.41	5.43



Fusion Reaction	$E_{c.m.} = 95.0 \text{ MeV}$		$E_{c.m.} = 107.6 \text{ MeV}$	
	$V_b \text{ (MeV)}$	$V_{com.} \text{ (MeV)}$	$V_b \text{ (MeV)}$	$V_{com.} \text{ (MeV)}$
$^{40}\text{Ca} + ^{90}\text{Zr}$	85.2	44.97	88.1	44.92
$^{40}\text{Ca} + ^{96}\text{Zr}$	80.6	45.38	88.2	45.29
$^{48}\text{Ca} + ^{90}\text{Zr}$	84.4	45.21	85.4	45.03

